Supporting Information

Scalable one-step electrochemical deposition of nanoporous amorphous S-doped $NiFe_2O_4/Ni_3Fe$ composite films as highly efficient electrocatalysts for oxygen evolution with ultrahigh stability

M.Y. Gao[a], J.R. Zeng[a], Q.B. Zhang[a,b*], C. Yang[a], X.T. Li[a], Y.X. Hua[a,b], C.Y. Xu[a,b]

[a] Key Laboratory of Ionic Liquids Metallurgy, Faculty of Metallurgical and Energy Engineering, Kunming University of Science and Technology, Kunming, 650093, P.R. China

[b] State Key Laboratory of Complex Nonferrous Metal Resources Cleaning Utilization in Yunnan Province, Kunming 650093, P.R. China

*Corresponding author. Tel: +86-871-65162008; fax: +86-871-65161278.

E-mail address: qibozhang@kmust.edu.cn (Q.B. Zhang)

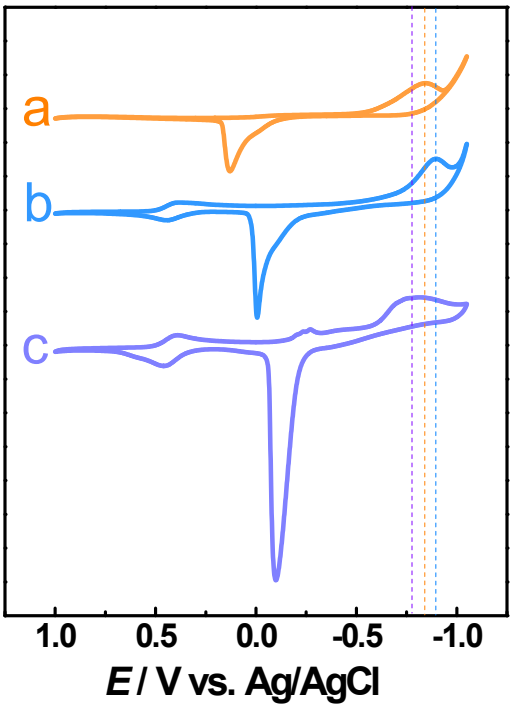

Figure S1. CVs of ethaline with (a) 100 mM $NiCl_2 \cdot 6H_2O$ (orange line), (b) 100 mM $NiCl_2 \cdot 6H_2O$ and 30 mM $FeCl_3 \cdot 6H_2O$ (blue line), (c) 100 mM $NiCl_2 \cdot 6H_2O$, 30 mM $FeCl_3 \cdot 6H_2O$ and 20 mM thiourea (purple line), respectively, recorded on Pt disk electrode under a scan rate of 20 mV s^{-1} at 333 K. In the binary system with both Ni(II) and Fe(III), the cathodic peak is found to negatively shift (ca. 50 mV), while the stripping wave belonging to the Ni dissolution is positively moved (ca. 120 mV). The extra redox couple peaks (at around 0.45 and 0.40 V), is associated with the oxidation/reduction of Fe(II)/Fe(III). The change on anodic process reveals the co-deposition of Ni and Fe, which is consist with the XRD result. In contrast, the introduction of S (20 mM thiourea) leads to obvious shift in the co-deposition potential to positive direction (ca. 120 mV), suggesting the promotion effect of S-doping on the electrochemical co-deposition of Ni-Fe alloy.

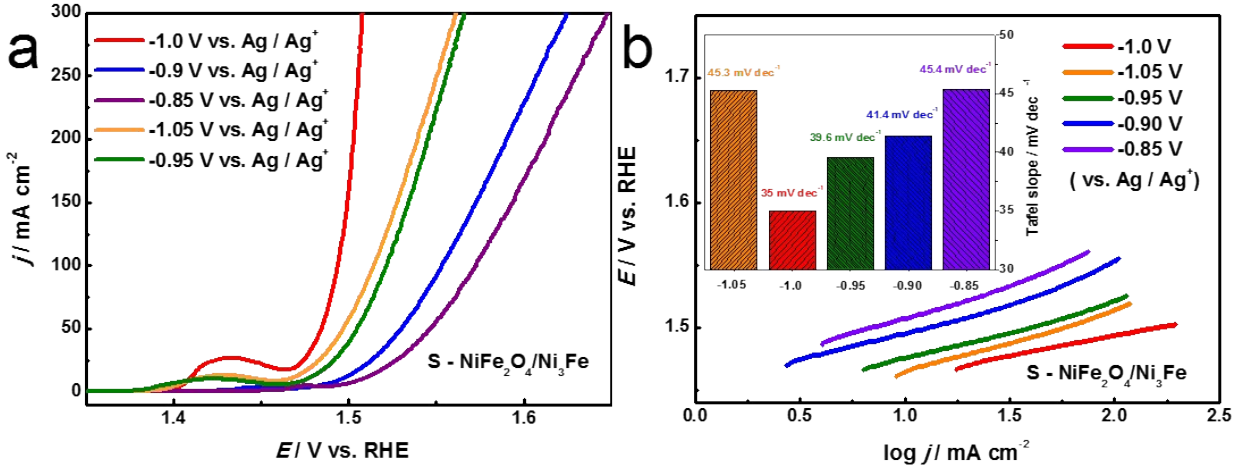

Figure S2. (a) The Linear sweep voltammograms (LSV) polarization curves in 1.0 M KOH solution at a scan rate of 2 mV s^{-1} of S-$NiFe_2O_4$/Ni_3Fe/NW films obtained from Ethaline containing 100 mM $NiCl_2 \cdot 6H_2O$, 30 mM $FeCl_3 \cdot 6H_2O$ and 20 mM thiourea at various electrodeposition potentials with a charge density of 5 C cm^{-2}. (b) The corresponding Tafel plots (inset: histogram of Tafel slopes).

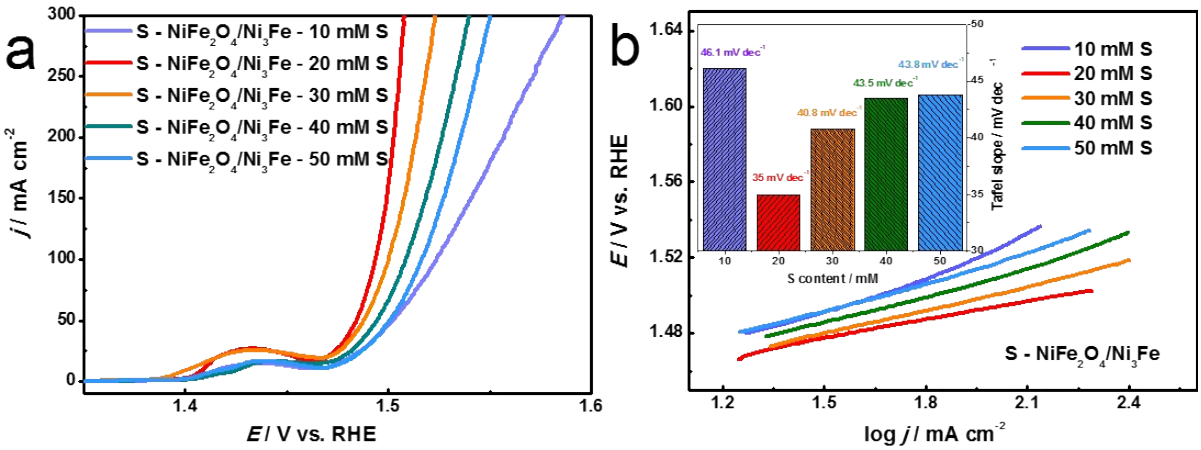

Figure S3. (a) The Linear sweep voltammograms (LSV) polarization curves in 1.0 M KOH solution at a scan rate of 2 mV s^{-1} of S-$NiFe_2O_4/Ni_3Fe$/NW films obtained in Ethaline containing 100 mM $NiCl_2{\cdot}6H_2O$ and 30 mM $FeCl_3{\cdot}6H_2O$ with different thiourea added concentrations (as indicated) at -1.0 V vs. Ag/Ag^+ with a charge density of 5 C cm^{-2}. (b) the corresponding Tafel plots (inset: histogram of Tafel slopes).

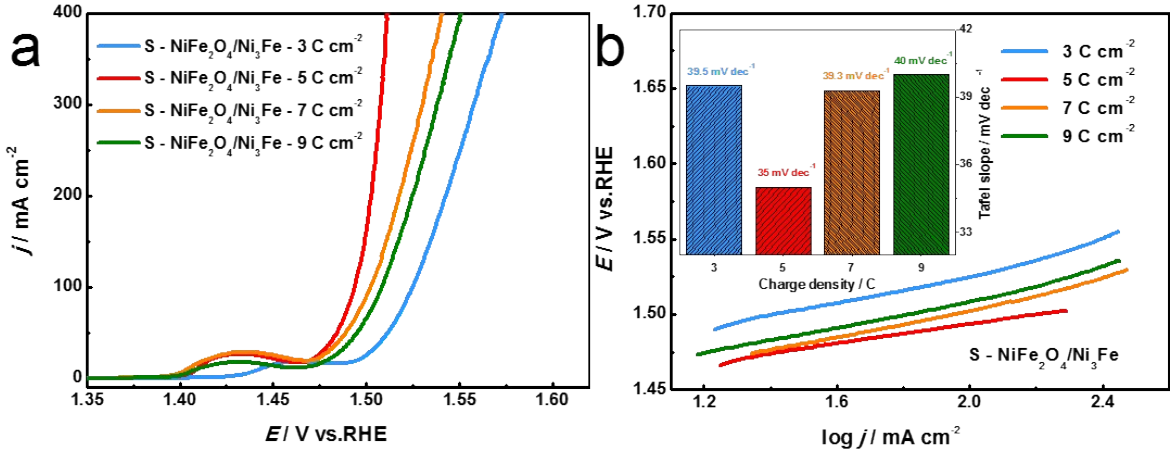

Figure S4. (a) The Linear sweep voltammograms (LSV) polarization curves of S-$NiFe_2O_4/Ni_3Fe$/NW films obtained from Ethaline containing 100 mM $NiCl_2{\cdot}6H_2O$, 30 mM $FeCl_3{\cdot}6H_2O$ and 20 mM thiourea with various charge densities (3 C cm^{-2}, 5 C cm^{-2}, 7 C cm^{-2}, 9 C cm^{-2}) in 1.0 M KOH solution at a scan rate of 2 mV s^{-1}. (b) The corresponding Tafel plots (inset: histogram of Tafel slopes).

It was found that the catalytic activity of the resultant samples highly depends on the deposition potential, added amount of thiourea, as well as charge density (Figures S2-S4). The optimal concentration of adding thiourea was found to be 0.02 M and the deposit prepared at -1.0 V vs. Ag/Ag^+ with a charge density of 5 C cm^{-2} yielded the highest OER catalytic activity, which possesses the minimum onset potential (ca. 240 mV) and maximum current flow with smaller Tafel slope (35 mV dec^{-1}).

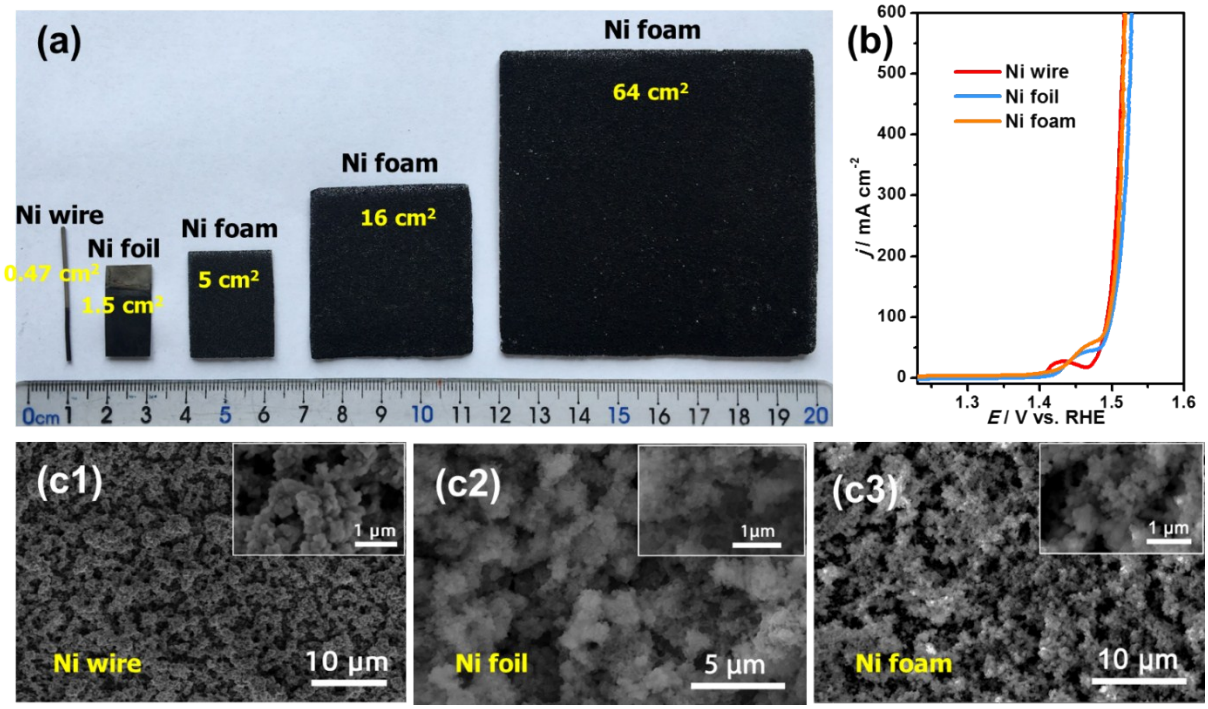

Figure S5. (a) Photographs and SEM images of S-$NiFe_2O_4$/Ni_3Fe/NW (prepared at -1.0 V vs. Ag/Ag^+ with a charge density of 5 C cm^{-2} at 333 K in Ethaline containing 100 mM $NiCl_2 \cdot 6H_2O$, 30 mM $FeCl_3 \cdot 6H_2O$ and 20 mM thiourea) grown on various nickel based substrates (including Ni wire, Ni foil, and Ni foam) with different scales (from 0.47 to 64 cm^2). (b) The corresponding LSV curves performed in 1.0 M KOH at 298 K with a scan rate of 2 mV s^{-1}. These results reveal that the shape and size of substrate have little influence on the resultant deposit morphology and associated OER catalytic performance, suggesting the generality of this facile and scalable one-step electrodeposition synthesis route in Ethaline. The Ni wire was chosen as the substrate to reflect the real catalytic activity of the prepared S-$NiFe_2O_4$/Ni_3Fe composite films, while the penetrating diffusion issue of electrolyte associated with the bulk foil substrate made some hindering effect on the catalytic performance. For porous substrates, such as foam, fiber, etc., can offer more contact area, easy diffusion term of electrolyte as well as more active species. However, it is critical to distinguish the intrinsic activity normalized to the geometric area and the actual area of the electrode. In fact, it is still urgent to seek specific catalyst activity normalized to actual catalyst surface area.

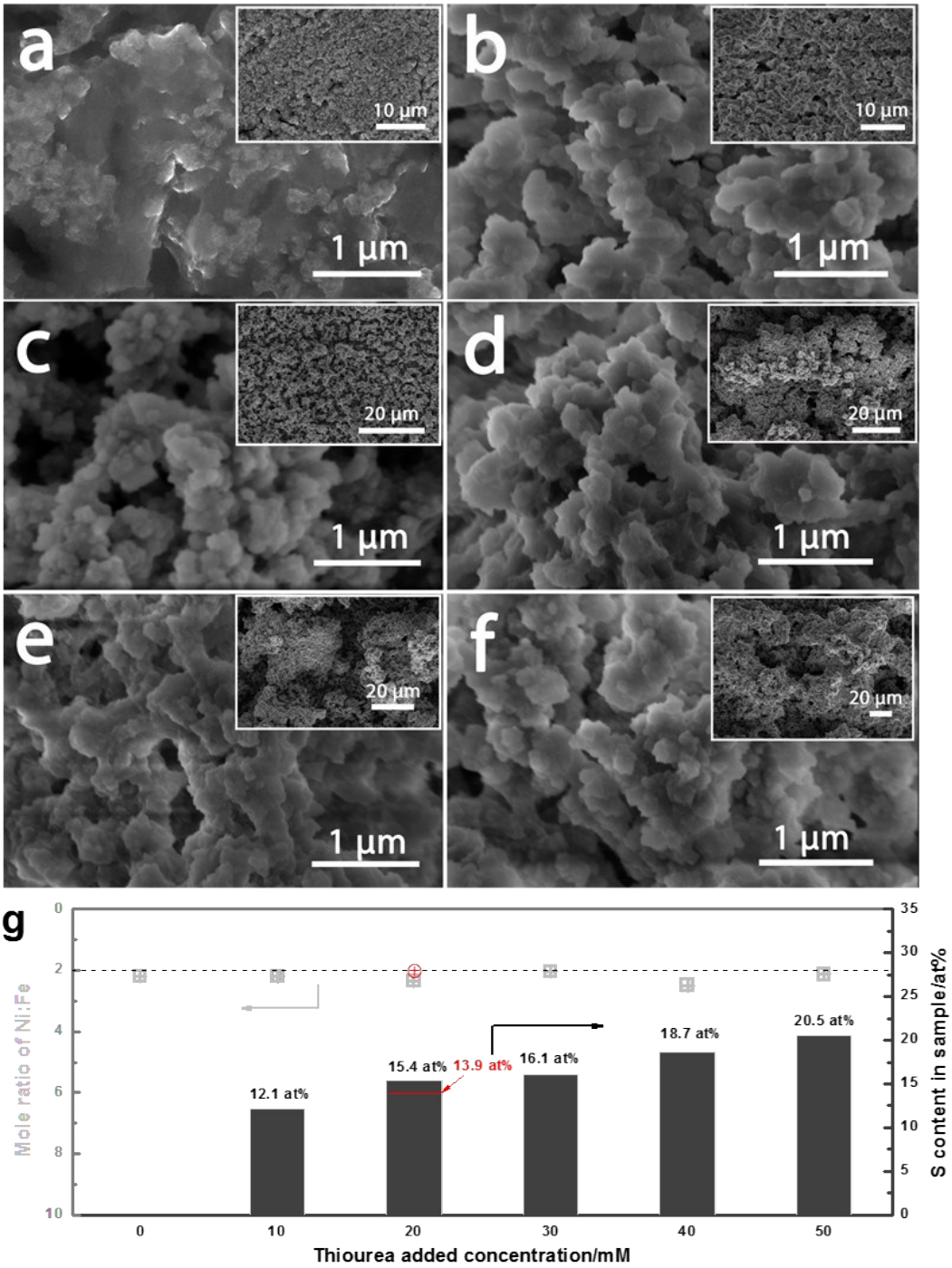

Figure S6. The low- and high-magnification SEM images of S-$NiFe_2O_4$/Ni_3Fe obtained at various thiourea added concentrations. (a) 0 mM, (b) 10 mM, (c) 20 mM, (d) 30 mM, (e) 40 mM, (f) 50 mM. (g) ICP-MS surveys of the corresponding samples. The result of the sample prepared with adding of 20 mM thiourea after long-term electrolysis was outlined in red. Note that the S doping shows negligible effect on the mole ratio of Ni/Fe (ca. 2:1), while results in marked changes on the surface structure. Increasing the added amount of thiourea (increasing S dopant concentrations in the samples) exceeded to 20 mM, the excessive growth of the active crystals is evident, which vertically developed to form clusters and resulted in poor structural adhesion and low electrical conductivity, particularly when the added thiourea concentration was increased to 40 or 50 mM.

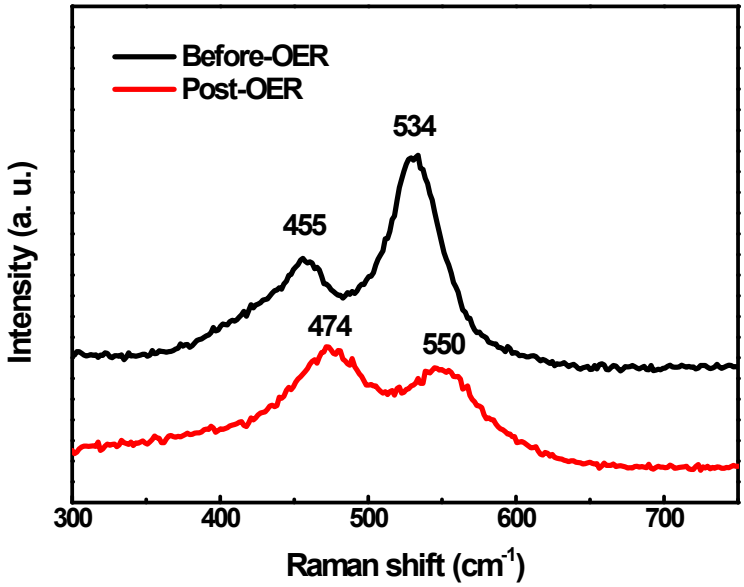

Figure S7. Raman spectra of S-$NiFe_2O_4/Ni_3Fe$/NW before-OER (black) and post-OER (red). The Raman bands at 474 and 550 cm^{-1} indicate the formation of NiOOH during the OER process, which is the oxidized product of $Ni(OH)_2$.

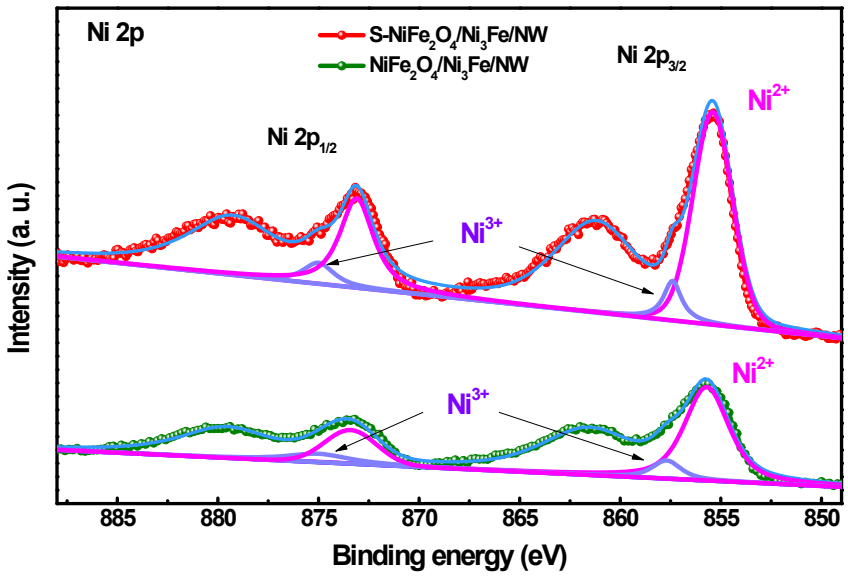

Figure S8. The fine-scanned Ni 2p spectra for $NiFe_2O_4/Ni_3Fe$ composites before and after S-doping. The two peaks with binding energies at 855.4 and 873.1 eV corresponded to the Ni^{2+}, with two satellite peaks at approximately 861.2 and 879.3 eV. The peaks located at 857.4 and 875.0 eV are ascribed to the presence of the Ni^{3+} oxidation state on the surface. The intense Ni^{2+} peaks indicate that the majority of Ni elements at the surface are Ni^{2+} cations. Further quantitative analysis indicates that the atomic ratio of Ni^{2+}/Ni^{3+} in $NiFe_2O_4/Ni_3Fe$ is 2.78, while that for S-$NiFe_2O_4/Ni_3Fe$ is 6.75.

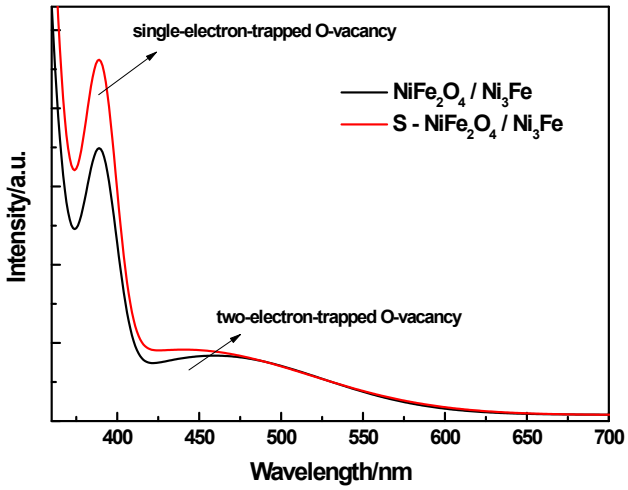

Figure S9. The photoluminescence (PL) spectra for $NiFe_2O_4/Ni_3Fe$ composites before and after S-doping. The PL emission peak at around 390 nm could be associated with the recombination of holes with single-electron-trapped oxygen vacancy, and the wide but noticeable peak at around 440-450 nm could be mainly attributed to the recombination of the photogenerated holes with the two-electron-trapped O-vacancy.[1-4] The more intensive peak obtained for S-$NiFe_2O_4/Ni_3Fe$ suggests more oxygen vacancies existing in the sample surface.

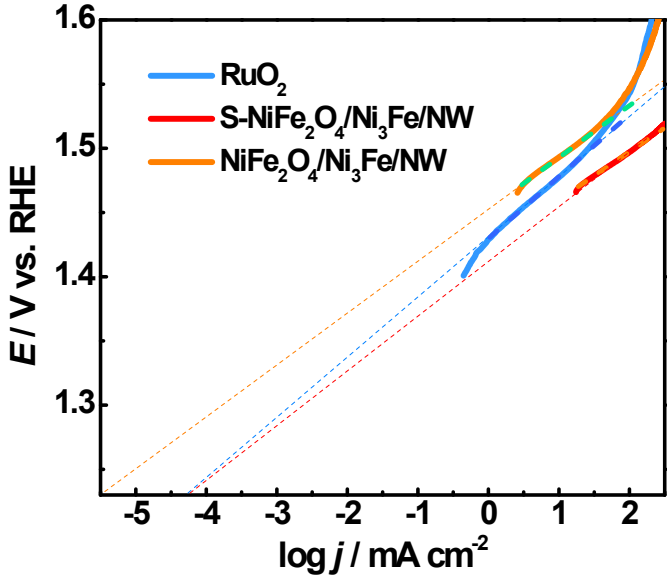

Figure S10. Calculated exchange current density of S-$NiFe_2O_4/Ni_3Fe$/NW, $NiFe_2O_4/Ni_3Fe$/NW, and commercial RuO_2 by applying extrapolation method to the Tafel plot.

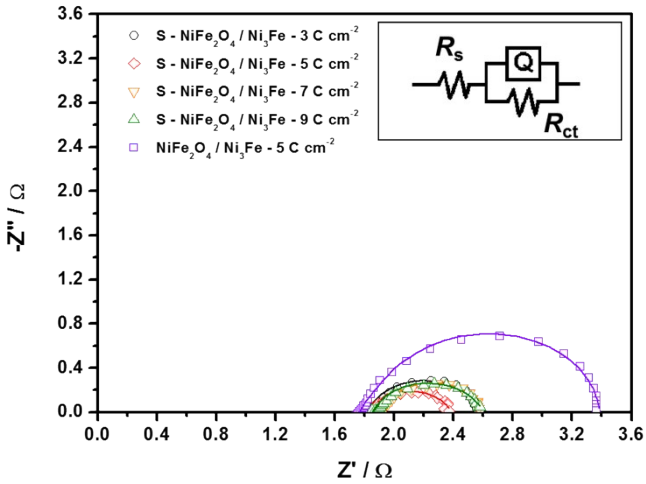

Figure S11. Nyquist plots at a constant overpotential of 300 mV for $NiFe_2O_4/Ni_3Fe$/NW and S-$NiFe_2O_4/Ni_3Fe$/NW electrode obtained at various charge densities (as indicated). The equivalent circuit used was shown in the inset, where R_s is the solution resistance, Q is the constant phase element, R_{ct} is the corresponding charge transfer resistance. The S-doped composite electrodes with various charge densities show much lower R_{ct} than $NiFe_2O_4/Ni_3Fe$/NW, and the S-$NiFe_2O_4/Ni_3Fe$/NW sample obtained with 5 C cm^{-2} exhibits the lowest charge transport resistance and fastest transfer kinetics.

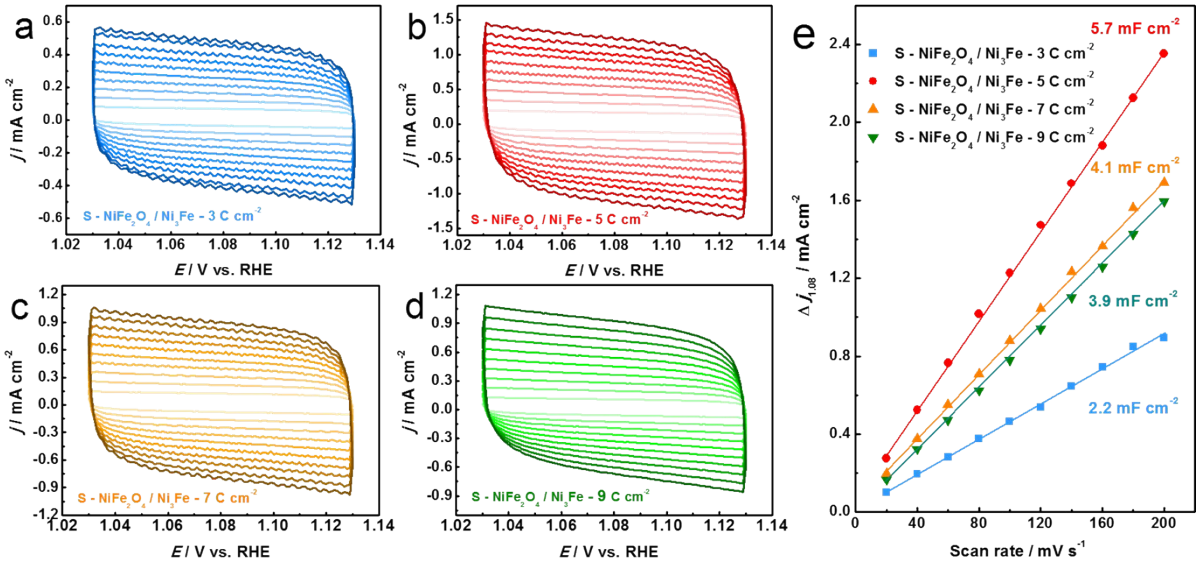

Figure S12. (a) Current density for S-$NiFe_2O_4/Ni_3Fe$/NW and $NiFe_2O_4/Ni_3Fe$/NW at 1.08V vs. RHE ($\Delta j = j_a - j_c$) plots depend on differences scan rate.

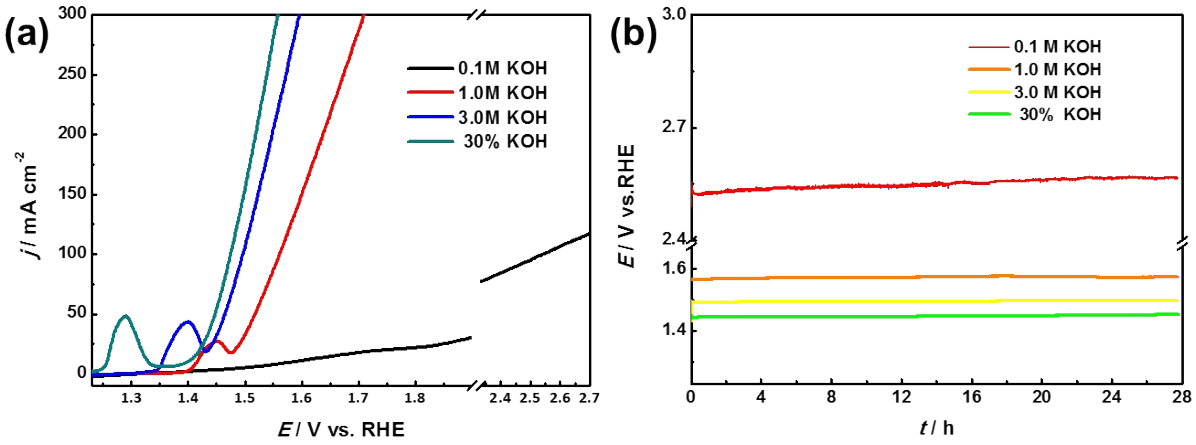

Figure S13. (a) LSV curves of S-$NiFe_2O_4$/Ni_3Fe/NW for OER in alkaline solutions with various KOH concentrations as indicated. (b) The corresponding chronopotentiometric curve for S-$NiFe_2O_4$/Ni_3Fe/NW operated at a constant current density of 100 mA cm^{-2} at 298 K.

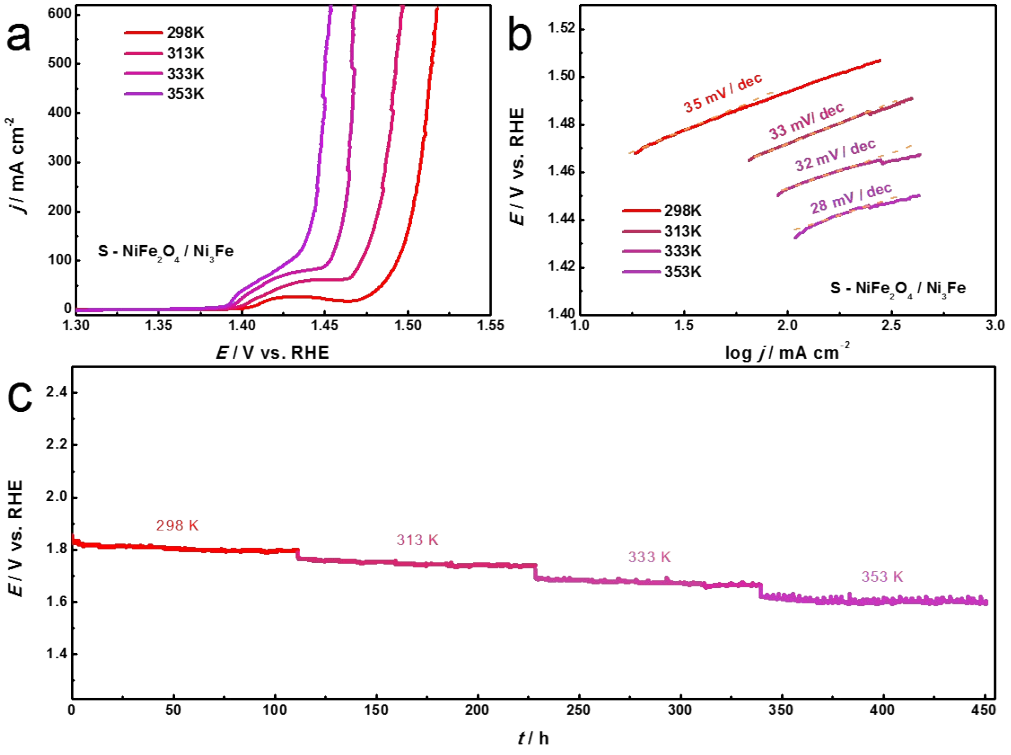

Figure S14. (a) Polarization curves for S-$NiFe_2O_4$/Ni_3Fe/NW at different temperatures in 1.0 M KOH (IR corrected). (b) The corresponding Tafel plots for S-$NiFe_2O_4$/Ni_3Fe/NW. (c) Chronopotential curves for S-$NiFe_2O_4$/Ni_3Fe/NW recorded at a fixed current density of 500 mA cm^{-2} for OER over 450 h at different temperatures (as indicated) in 1.0 M KOH (without iR correction).

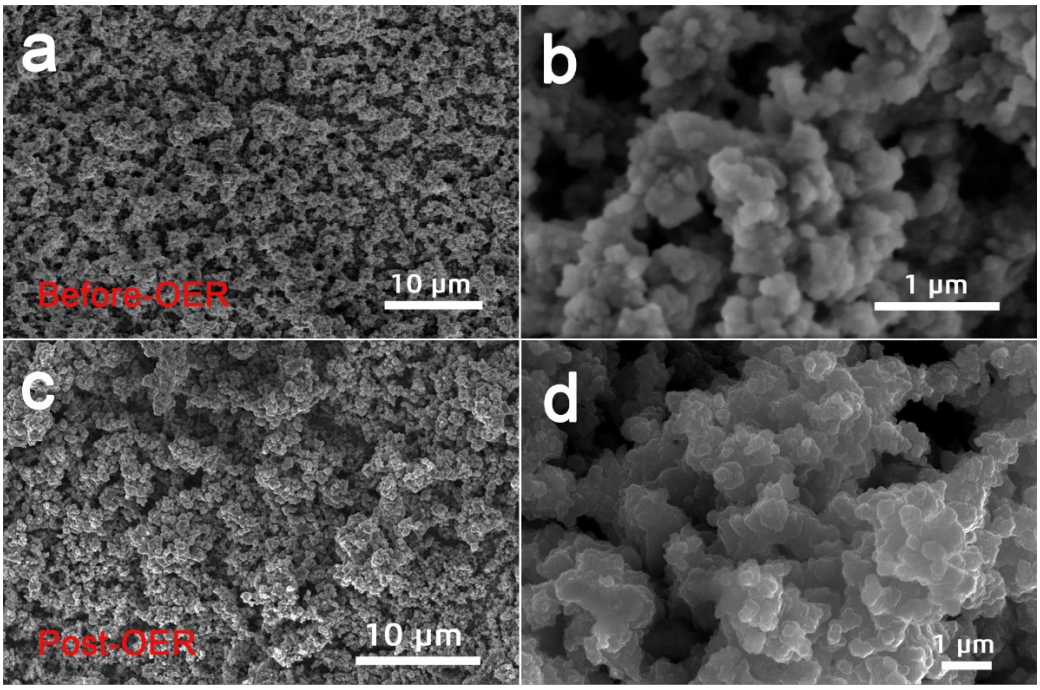

Figure S15. Comparison of SEM of S-$NiFe_2O_4$/Ni_3Fe before (a) and after (c) long-term electrolysis (at j = 100 mA cm^{-2} for 110 h) for OER in 1.0 M KOH at 298 K, the corresponding high-magnification SEM images of (b) and (d), respectively.

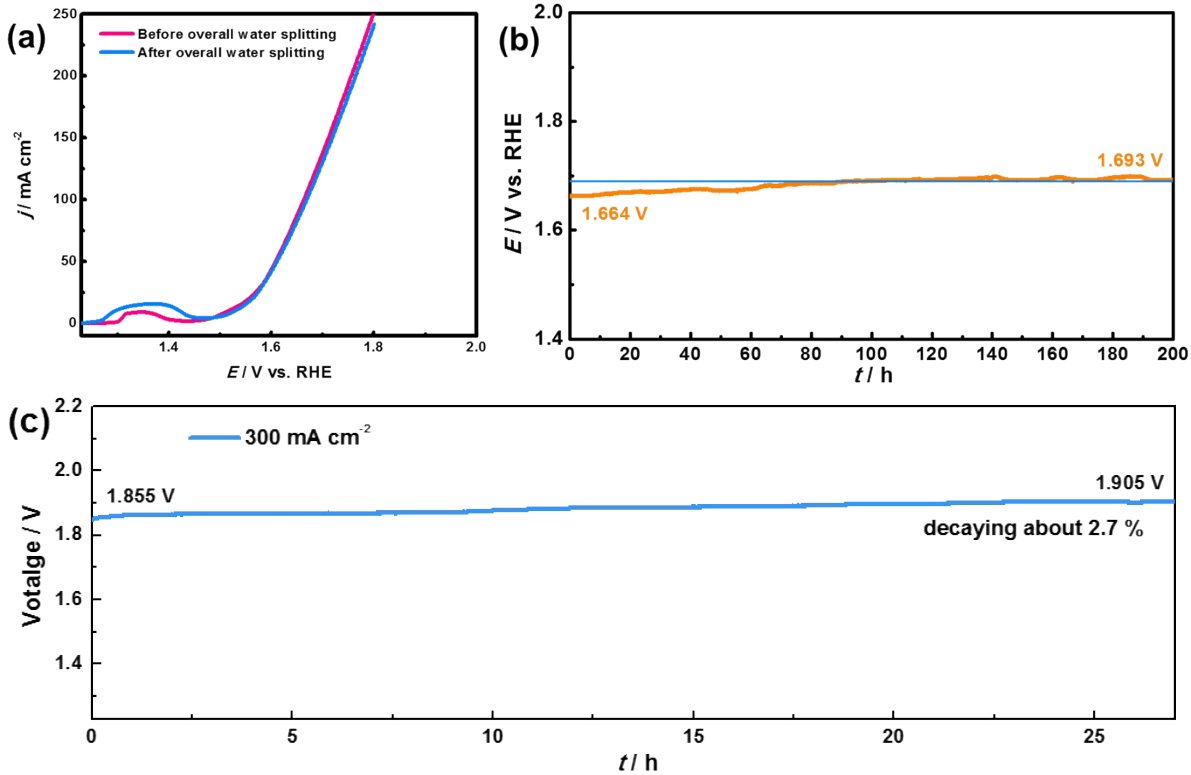

Figure S16. (a) LSV curves of S-$NiFe_2O_4$/Ni_3Fe/NW||Ni-Mo MS/NW catalyst couple before and after 200 h overall water splitting stability test. Chronopotentiometry curves of the S-$NiFe_2O_4$/Ni_3Fe/NW||Ni-Mo MS/NW operated at constant current densities of (b) 100 mA cm^{-2} at 298 K for 200 h and (c) 300 mA cm^{-2} at 298 K for 27 h. All data were obtained in 30 wt% KOH at 298 K without iR correction.

Table S1. Comparison of some representative Ni-based OER catalysts recently reported for basic solutions.

Catalyst	Electrolyte	Overpotential /mV @100 mA cm^{-2}	Ref.
S-$NiFe_2O_4$/Ni_3Fe/NW	1.0 M KOH	260	This work
Ni_3Se_2/Cu foam	1.0 M KOH	450	[5]
NiFe LDH/Ni foam	1.0 M NaOH	450	[6]
NiS/Ni foam	1.0 M KOH	360	[7]
NiSe/Ni foam	1.0 M KOH	320	[8]
Ni_3Se_2 /Ni foam	1.0 M KOH	353	[9]
Fe-NiSe/FeNi foam	1.0 M KOH	264	[10]
$Ni_{0.33}Co_{0.67}S_2$/CC	1.0 M KOH	370	[11]
$NiCo_2S_4$/CC	1.0 M KOH	340	[12]
NiP/Cu foam	1.0 M KOH	460	[13]
Ni/NiP	1.0 M KOH	320	[14]
NiMo/TiM	1.0 M KOH	360	[15]
MoS_2–Ni_3S_2 HNRs/NF	1.0 M KOH	340	[16]
MoS_2/Ni_3S_2	1.0 M KOH	300	[17]
V/nickel foam	1.0 M KOH	370	[18]
Amorphous $Ni_{40}Fe_{40}P_{20}$	1.0 M NaOH	~360	[19]
FeNiP/rGO-400	1.0 M KOH	~380	[20]
Ni-Fe-P-350	1.0 M KOH	>350	[21]
M-Ni_2P/Fe_2P-O	1.0 M KOH	251	[22]
Cu@NiFe LDH coreshell/Cu foam	1.0 M KOH	281	[23]

Table S2 Comparison of different Ni-based catalysts for overall water splitting with recently reported works.

Catalyst	Electrolyte	Voltage @10 mA cm^{-2}	Voltage @100 mA cm^{-2}	Stability test	Ref.
S-$NiFe_2O_4$/Ni_3Fe/NW	1.0 M KOH	1.52 V	1.79 V	220 h	This work
S-$NiFe_2O_4$/Ni_3Fe/NW	30 wt% KOH	—	1.69 V	200 h	This work
NiFe LDH/Ni foam||NiFe LDH/Ni foam	1.0 M NaOH	1.70 V			[6]
NiP/Cu foam||NiP/Cu foam	1.0 M KOH	1.56 V		15 h	[13]
Ni_5P_4/Ni foil||Ni_5P_4/Ni foil	1.0 M KOH	1.70 V			[24]
Ni_2P/GC||Ni_2P/GC	1.0 M KOH	1.63 V		10 h	[25]
NiMo/TiM||NiMo/TiM	1.0 M KOH	1.64 V		10 h	[15]
NiS/Ni foam|| NiS/Ni foam	1.0 M KOH	1.64 V		35 h	[7]
NiSe/Ni foam||NiSe/Ni foam	1.0 M KOH	1.63 V		20 h	[8]
$NiCo_2S_4$@NiFe/Ni foam|| $NiCo_2S_4$@NiFe/Ni foam	1.0 M KOH	1.60 V		12 h	[26]
NiO/Ni foam ||Ni_2P/Ni foam	1.0 M KOH	1.65 V		120 h	[27]
MoS_2-Ni_3S_2 HNRs/NF|| MoS_2-Ni_3S_2 HNRs/NF	1.0 M KOH	1.50 V		48 h	[16]
MoS_2/Ni_3S_2 particles	1.0 M KOH	1.56 V		10 h	[17]
Ni/NiP||Ni/NiP	1.0 M KOH	1.61 V		4 h	[14]
V/nickel foam||V/nickel foam	1.0 M KOH	1.74 V		24 h	[18]
$Ni_{2.5}Co_{0.5}Fe$/NF|| $Ni_{2.5}Co_{0.5}Fe$/NF	1.0 M KOH	1.62 V	~1.89 V	--	[28]
$Ni_xCo_{3x}O_4$||$Ni_xCo_{3-x}O_4$	1.0 M KOH	1.75 V		10 h	[29]
NiFe/$NiCo_2O_4$/NF||NiFe/$NiCo_2O_4$/NF	1.0 M KOH	1.67 V	~1.88 V	10 h	[30]
EG/$Co_{0.85}Se$/NiFe|| EG/$Co_{0.85}Se$/NiFe	1.0 M KOH	1.67 V		10 h	[31]
Cu@NiFe LDH coreshell/Cu foam	1.0 M KOH	1.54 V	1.69 V	48 h	[23]
Ni-Fe-P-350 Nanocubes	1.0 M KOH	1.67 V		40 h	[21]
S-$NiFe_2O_4$/nickel foam nanosheets	1.0 M KOH	1.65 V		24 h	[32]

Reference

[1] G. S. Huang, X. L. Wu, Y. F. Mei, X. F. Shao, *J. Appl. Phys.* 2003, **93**, 582

[2] F. Lei, Y. Sun, K. Liu, S. Gao, L. Liang, B. Pan, Y. Xie, *J. Am. Chem. Soc*. 2014, **136**, 6826.

[3] J. Bao, X. D. Zhang, B. Fan, J. J. Zhang, M. Zhou, W. L. Yang, X. Hu, H. Wang, B. C. Pan, Y. Xie, *Angew. Chem., Int. Ed.*, 2015, **127**, 7507-7512.

[4] L. Zhuang, L. Ge, Y. Yang, M. Li, Y. Jia, X. Yao, Z. Zhu, *Adv. Mater.*, 2017, 29.

[5] J. L. Shi, J. M. Hu, Y. L. Luo, X. P. Sun, A. M. Asiri, *Catal. Sci. Technol.,* 2015, **5**, 4954-4958.

[6] J. I. Luo, J. H. Im, M. T. Mayer, M. Schreier, M. K. Nazeeruddin, N. G. Park, S. D. Tilley, H. J. Fan, M. Grätzel, *Science,* 2014, **345**, 1593-1596.

[7] W. Zhu, X. Yue, W. Zhang, S. Yu, Y. Zhang, J. Wang, J. Wang, *Chem. Commun.,* 2016, 52, 1486-9.

[8] C. Tang, N. Y. Cheng, Z. H. Pu, W. Xing, X. P. Sun, *Angew. Chem. Int. Edit.,* 2015, **54**, 9351-5.

[9] R. Xu, R. Wu, Y. Shi, J. Zhang, B. Zhang, *Nano Energy,* 2016, **24**, 103-110.

[10] C. Tang, A. M. Asirib, X. P. Sun, *Chem. Commun.,* 2016, **52**, 4529-4532.

[11] W. Fang, D. Liu, Q. Lu, X. Sun, A. M. Asiri, *Electrochem. Commun.,* 2016, **63**, 60-64.

[12] D. N. Liu, Q. Lu, Y. L. Luo, X. P. Sun, A. M. Asiri, *Nanoscale,* 2015, **7**, 15122-15126.

[13] Q. Liu, S. Gu, C. M. Li, *J. Power Sources,* 2015, **299**, 342-346.

[14] G.-F. Chen, T. Y. Ma, Z.-Q. Liu, N. Li, Y.-Z. Su, K. Davey, S.-Z. Qiao, *Adv. Funct. Mater.,* 2016, **26**, 3314-3323.

[15] J. Tian, N. Cheng, Q. Liu, X. Sun, Y. He, A. M. Asiri, *J. Mater. Chem. A,* 2015, **3**, 20056-20059.

[16] Y. Yang, K. Zhang, H. Lin, X. Li, H. C. Chan, L. Yang, Q. Gao, *ACS Catal.,* 2017, **7**, 2357-2366.

[17] J. Zhang, T. Wang, D. Pohl, B. Rellinghaus, R. Dong, S. Liu, X. Zhuang, X. Feng, *Angew. Chem.,* 2016, **55**, 6702-7.

[18] Y. Yu, P. Li, X. Wang, W. Gao, Z. Shen, Y. Zhu, S. Yang, W. Song, K. Ding, *Nanoscale,* 2016, **8**, 10731-10738.

[19] F. Hu, S. Zhu, S. Chen, Y. Li, L. Ma, T. Wu, Y. Zhang, C. Wang, C. Liu, X. Yang, L. Song, X. Yang, Y. Xiong, *Adv. Mater.,* 2017, **29**, 1606570.

[20] X. Fang, L. Jiao, R. Zhang, H. L. Jiang, *ACS Appl. Mater. Inter.,* 2017, **9**, 23852-23858.

[21] C. Xuan, J. Wang, W. Xia, Z. Peng, Z. Wu, W. Lei, K. Xia, H. L. Xin, D. Wang, *ACS Appl. Mater. Inter.,* 2017, **9,** 26134-26142.

[22] P. F. Liu, X. Li, S. Yang, M. Y. Zu, P. Liu, B. Zhang, L. Zheng, H. Zhao, H. G. Yang, *ACS Energy Lett.,* 2017, **2**, 2257–2263.

[23] L. Yu, H. Zhou, J. Sun, F. Qin, F. Yu, J. Bao, Y. Yu, S. Chen, Z. Ren, *Energ. Environ. Sci.,* 2017, **10**, 1820-1827.

[24] M. Ledendecker, S. Krick Calderon, C. Papp, H. P. Steinruck, M. Antonietti, M. Shalom, *Angew. Chem.,* 2015, **54**, 12361-5.

[25] L.-A. Stern, L. Feng, F. Song, X. Hu, *Energ. Environ. Sci.,* 2015, **8**, 2347-2351.

[26] J. Liu, J. Wang, B. Zhang, Y. Ruan, L. Lv, X. Ji, K. Xu, L. Miao, J. Jiang, *ACS Appl. Mater. Inter.,* 2017, **9**, 15364-15372.

[27] J. Zheng, W. Zhou, T. Liu, S. Liu, C. Wang, L. Guo, *Nanoscale,* 2017, **9**, 4409-4418.

[28] X. Zhu, C. Tang, H.-F. Wang, B.-Q. Li, Q. Zhang, C. Li, C. Yang, F. Wei, *J. Mater. Chem. A,* 2016, **4**, 7245-7250.

[29] X. Yan, K. Li, L. Lyu, F. Song, J. He, D. Niu, L. Liu, X. Hu, X. Chen, *ACS Appl. Mater. Inter.,* 2016, **8**, 3208-14.

[30] C. L. Xiao, Y. B. Li, X. Y. Lu, C. Zhao, *Adv. Funct. Mater.,* 2016, **26**, 3515-3523.

[31] Y. Hou, M. R. Lohe, J. Zhang, S. H. Liu, X. D. Zhuang, X. L. Feng, *Energ. Environ. Sci.,* 2016, **9**, 478-483.

[32] J. Liu, D. Zhu, T. Ling, A. Vasileff, S.-Z. Qiao, *Nano Energy,* 2017, DOI: 10.1016/j.nanoen.2017.08.031.